

Geometric Modeling of Cutter/Workpiece Engagements in Three-Axis Milling Using Polyhedral Representations

Eyyup Aras

Department of Mechanical Engineering,
University of British Columbia,
1000 University Boulevard,
Vancouver, BC, V6T 1Z4, Canada
e-mail: araseyy@interchange.ubc.ca

Derek Yip-Hoi

Department of Engineering Technology,
Western Washington University,
312 Ross Engineering Building,
512 Main Street,
Bellingham, WA 98225
e-mail: derek.yip-hoi@wwu.edu

Modeling the milling process requires cutter/workpiece engagement (CWE) geometry in order to predict cutting forces. The calculation of these engagements is challenging due to the complicated and changing intersection geometry that occurs between the cutter and the in-process workpiece. This geometry defines the instantaneous intersection boundary between the cutting tool and the in-process workpiece at each location along a tool path. This paper presents components of a robust and efficient geometric modeling methodology for finding CWEs generated during three-axis machining of surfaces using a range of different types of cutting tool geometries. A mapping technique has been developed that transforms a polyhedral model of the removal volume from the Euclidean space to a parametric space defined by the location along the tool path, the engagement angle, and the depth of cut. As a result, intersection operations are reduced to first order plane-plane intersections. This approach reduces the complexity of the cutter/workpiece intersections and also eliminates robustness problems found in standard polyhedral modeling and improves accuracy over the Z-buffer technique. The CWEs extracted from this method are used as input to a force prediction model that determines the cutting forces experienced during the milling operation. The reported method has been implemented and tested using a combination of commercial applications. This paper highlights ongoing collaborative research into developing a virtual machining system.

[DOI: 10.1115/1.2960490]

Keywords: cutter/workpiece engagements, virtual machining, polyhedral models, 3-axis milling, swept volumes

1 Introduction

One of the steps in simulating machining operations is the accurate extraction of the intersection geometry between the cutting tool and the workpiece during machining. Given that industrial machined components can have highly complex workpiece and cutting tool geometries, extracting cutter/workpiece engagement (CWE) geometry accurately and efficiently is challenging. Figure 1 summarizes the steps involved in CWE extraction. Inputs from computer aided design (CAD)/CAM include the tool paths in the form of a cutter location data (CL data) file, a geometric description of the cutting tool, and a geometric representation (B-rep, polyhedral, Z-buffer model) of the initial workpiece.

CWE geometry is a key input to force calculations and feed rate scheduling in milling operations. This geometry defines the instantaneous intersection boundary between the cutting tool and the in-process workpiece at each location along a tool path. From the CWE, the cutter flute entry-exit angles and depth of cuts are found and are in turn used to calculate the instantaneous cutting forces in the radial, tangential, and feed directions. The task is relatively simple when cylindrical end mills and simple workpieces are used. However in practice this is often not the case. More often the tool and the workpiece geometries are much more complex. The most complicated CWE calculations occur during the machining of sculptured surfaces, e.g., automobile body part stamping dies.

In this paper a methodology is presented for finding the CWE

for three-axis milling that maps a polyhedral representation of the removal volume from a Euclidean space into a parametric space. The nature of the swept geometry and the goal of engagement extraction points toward a preferred parametrization. As shown in Fig. 2, the engagement (immersion) angle (ϕ), the depth of cut (d) for points on the cutter surface, and the tool tip distance ($L(t)$) make up this parametrization, $P(\phi, d, L(t))$, where ($0 \leq t \leq 1$).

This mapping, as will be seen, has the effect of reducing the cutting tool geometry to an unbounded plane. Thus the boundary of the CWE is found by performing first order intersections between the planar representation of the cutting tool and the planar facets in the polyhedral representation of the removal volume. Before presenting the details of the method, a literature review of related research in machining simulation and verification, CWE extraction, and process modeling is presented.

2 Literature Review

Geometric modeling techniques have been extensively used in verifying the correctness of NC tool paths. Some of these have been extended to extracting CWEs in support of physical simulation of the process that starts with the calculation of the cutting forces.

In geometric simulation, the dominant approaches are the vector based solutions [1–8]. Although mathematically more tractable than the solid modeler approach for example (which performs surface/surface intersections), as shown in Fig. 3, these techniques suffer from inaccuracies due to the rasterization effect common to many discretized problems [6]. Although accuracy is improved by increasing the resolution of the underlying grid, this comes with the expense of larger memory and computational requirements.

Contributed by the Computer Aided Product Development (CAPD) Committee for publication in the JOURNAL OF COMPUTING AND INFORMATION SCIENCE IN ENGINEERING. Manuscript received July 19, 2007; final manuscript received June 10, 2008; published online August 19, 2008. Assoc. Editor: J. Corney.

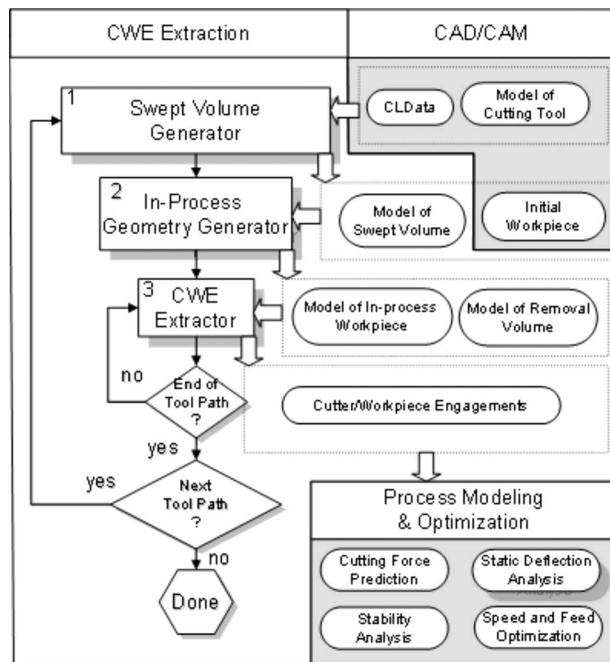


Fig. 1 CWE extraction

Research into solid modeler based methodologies has been reported [9–16]. In these approaches, in-process workpiece updating and cutter/workpiece engagement extraction are performed using geometric and topologic algorithms within the solid modeler kernel. Notwithstanding improvements in the efficiency and robustness of these algorithms in today's solid modeling kernels, the sheer number of such intersections that must be performed in simulating machining on a real part still makes this a difficult technology to deploy practically. Other limitations come for the size of the data structure that is necessary particularly for capturing relationships between topology. These relationships are preserved when using a solid modeler for small surface artifacts such as cusps that are generated during machining (Fig. 4). This results

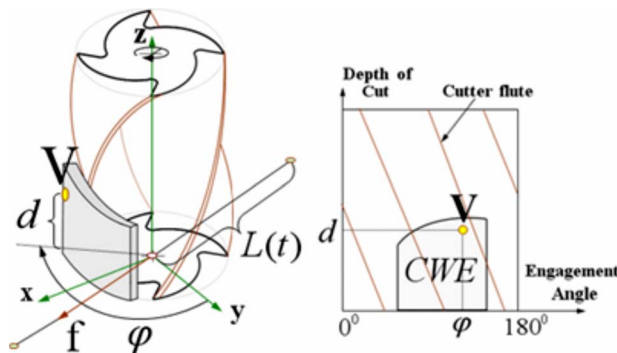


Fig. 2 CWE parameters

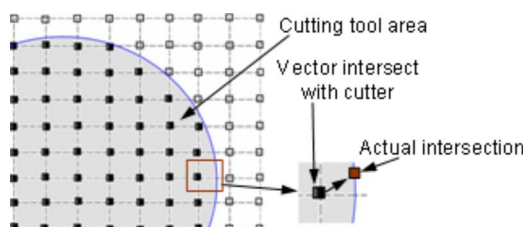


Fig. 3 Z-map calculation errors when the grid size is large

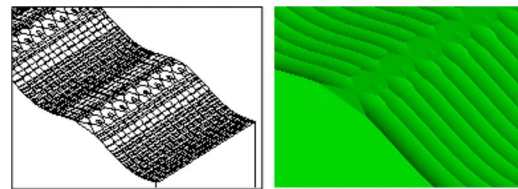


Fig. 4 Final machined surfaces with cusps

in a data structure that is large and that grows as the simulation progresses particularly when ball and bull-nose cutters are being used. Although research continues to use this technology, it remains to be seen whether it is practical.

Another representation for the workpiece geometry that is starting to receive more attention is the polyhedral model (see Fig. 5). This representation may offer a good compromise between manageable computational speed, robustness, and accuracy. These models have become pervasive in supporting engineering applications. They are found in all CAD applications as faceted models for visualization and are used extensively in simulation, CAE, and rapid prototyping.

The rest of the paper is organized as follows. An algorithm to obtain CWEs is presented in Sec. 3, followed by the implementation which contains a developed prototype system in Sec. 4 and examples in Sec. 5. Discussion and future work is presented in Sec. 6, and the paper is concluded in Sec. 7. In the Appendix the formulas of the CWE extraction methodology for different types of cutters are given.

3 Engagement Extraction Methodology

Polyhedral models provide the advantage of simplifying the workpiece surface geometry to planes which consist of linear boundaries. Thus for most cases the intersection calculations reduce to line/surface intersections. These can be performed analytically for the geometry found on cutting tools. For obtaining CWE area, facets which contain linear boundaries are intersected with the surface of the cutter and then the intersection points are connected to each other [17]. CWE extraction algorithms must be robust enough to handle the complete set of intersection cases between the cutting tool and a triangular facet (see Fig. 6(a)).

The faceting algorithm that generates this model approximates surfaces to a specified chordal error. As can be seen from the 2D view (Fig. 6(b)), this results in facets that lie outside the tool envelop at a given location even though the cutting tool is in contact with the actual removal volume surface. This facet should be considered in finding the CWE boundary but would be difficult to detect since it does not intersect with the tool geometry.

In finding engagement geometry, the following properties of the representations for swept and removal volumes in the parametric space $P(\phi, d, L(t))$ motivate finding the mapping $M: E^3 \rightarrow P(\phi, d, L)$

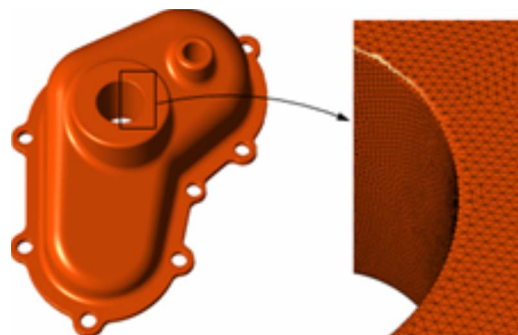


Fig. 5 Faceted representation of a model

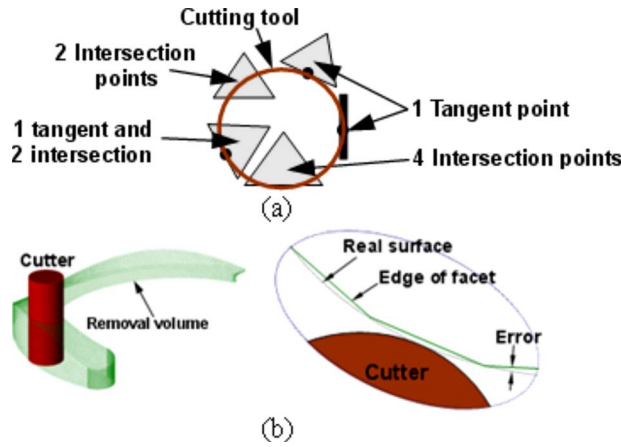


Fig. 6 Possible (a) cutter/facet engagements and (b) chordal error

Property 1. Given SV_i^P , a representation of the swept volume SV_i for tool path T_i in $P(\varphi, d, L(t))$, its intersection with an unbounded plane Q generates a closed set of points $CWE_K(t)$ on the surface of the cutter at location t along a tool path where $\mathbf{f} \cdot \mathbf{N} \geq 0$.

Property 2. Given RV_i^P , a representation of the removal volume RV_i for tool path T_i in $P(\varphi, d, L(t))$, its intersection with an unbounded plane Q generates a closed set of points $CWE(t) \subset CWE_K(t)$ that constitutes all points in engagement with the workpiece at location t along the tool path.

Of interest is the boundary set of $CWE(t)$ and $bCWE(t)$. This defines the geometry required for input to process modeling (i.e., force prediction). Thus, $bCWE(t) \subset CWE(t) \subset CWE_K(t)$. These three sets are illustrated in Fig. 7. The properties given above point to a novel approach for finding the engagement geometry, assuming that the mapping M can be constructed: Given RV_i^P generated by applying M to RV_i , $CWE(t)$ and $bCWE(t)$ can be found by intersecting RV_i^P with an unbounded plane for each cutter location defined by t .

The use of an unbounded plane in finding engagements eliminates the problem highlighted in Fig. 6(b) where the chordal error in the polyhedral representation of a removal volume introduces uncertainty in the intersection calculation. Further the reduction of the cutter surface geometry to a first order form simplifies intersection calculations, particularly when the removal volume is polyhedral.

3.1 Derivation of Mapping M for Linear Tool Path. In this section derivations of the mapping M used for obtaining engagements for cutting tools with natural quadrics and toroidal surfaces are developed. Natural quadrics (Fig. 8(a)) consist of the sphere, circular cylinder, and cone. Together with the plane (a degenerate quadric) and torus, these constitute the surface geometries found on the majority of cutters used in milling. For example a ball nose end mill (BNEM) is defined by two natural quadric surfaces—spherical and cylindrical. Other examples are shown in Fig. 8(b).

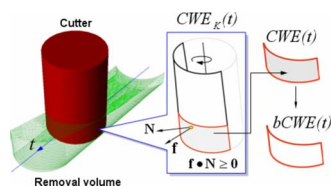


Fig. 7 Point sets $CWE_K(t)$, $CWE(t)$, and $bCWE(t)$ used in defining engagements

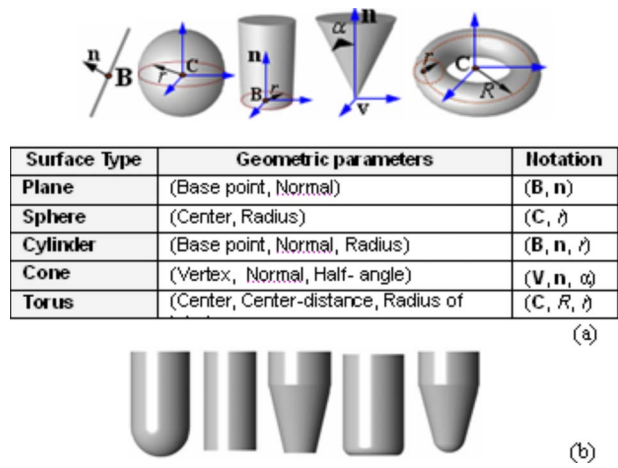


Fig. 8 Constituent surfaces of (a) milling cutters and (b) some typical milling cutter surfaces

In developing the mapping M , the *implicit equations* of the cutter geometries will be used. These are

$$\text{Sphere: } (\mathbf{P} - \mathbf{C}) \cdot (\mathbf{P} - \mathbf{C}) - r^2 = 0 \quad (1a)$$

$$\text{Cylinder: } (\mathbf{P} - \mathbf{B}) \cdot (\mathbf{P} - \mathbf{B}) - [(\mathbf{P} - \mathbf{B}) \cdot \mathbf{n}]^2 - r^2 = 0 \quad (1b)$$

$$\text{Cone: } [(\mathbf{P} - \mathbf{V}) \cdot \mathbf{n}]^2 - \cos^2(\alpha)(\mathbf{P} - \mathbf{V}) \cdot (\mathbf{P} - \mathbf{V}) = 0 \quad (1c)$$

$$\text{Torus: } [(\mathbf{P} - \mathbf{C}) \cdot (\mathbf{P} - \mathbf{C}) - r^2 - R^2]^2 + 4R^2[(z - z_C)^2 - r^2] = 0 \quad (1d)$$

$$\text{Plane: } (\mathbf{P} - \mathbf{B}) \cdot \mathbf{n} = 0 \quad (1e)$$

where \mathbf{P} represents the position of an arbitrary point on the cutter's surface and the coordinates of \mathbf{C} are x_C , y_C , and z_C . Derivations will be shown for the BNEM, and formulas for the other cutter types can be found in the Appendix. A BNEM is made up of a hemispherical and a cylindrical surface. Based on the kinematics of three-axis machining, subsets of these surfaces denoted as $CWE_{K,S}(t)$ and $CWE_{K,C}(t)$ will contribute to the set $CWE_K(t)$, as defined in the previous section, i.e., $CWE_K(t) = CWE_{K,S}(t) \cup CWE_{K,C}(t)$. In this section transformation formulas will be derived for the mapping of the hemispherical surface, M_{sphere} . The methodology and many of the formulas developed apply equally to the mapping for the cylindrical surface of the cutter, M_{cyl} . This will be further explained later in this section.

3.1.1 Derivation of Mapping M_{sphere} . In addition to the geometric definition of the surface, the location of a point on the cutter geometry as it moves along a tool path is also required. To do this the following terms are introduced (see Fig. 9).

(1) **WCS: Workpiece coordinate system ($\mathbf{i}, \mathbf{j}, \mathbf{k}$).** This is where

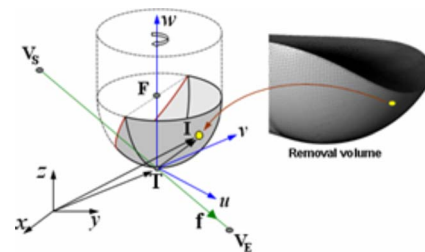


Fig. 9 Description of a point on a cutter moving along a tool path

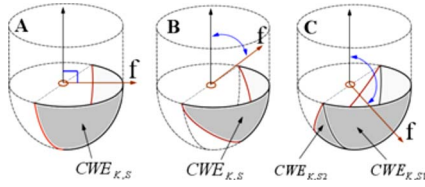


Fig. 10 Three-axis linear tool motions with a BNEM

the geometry of the removal volume and tool paths are defined.

- (2) TCS: Tool coordinate system ($\mathbf{u}, \mathbf{v}, \mathbf{w}$) positioned at the tool tip with \mathbf{w} along the cutter axis. It is assumed that the \mathbf{x} axis of the local tool coordinate system is aligned with the feed vector direction.
- (3) $\mathbf{T}(t)$: The position of the tool tip point (x_T, y_T, z_T, t) at t along tool path T_i in the WCS.
- (4) \mathbf{I} : The position of a point (x_I, y_I, z_I) on the cutter surface that belongs to the set $\text{CWE}_K(t)$ at t along tool path T_i in the WCS.
- (5) $\mathbf{F}(t)$: The position of a reference point (x_R, y_R, z_R, t) on the cutting tool axis at t along tool path T_i .

Feasible three-axis linear tool motions are shown in Fig. 10.

For motions **A** and **B** the engagement angle of a point at $\mathbf{I} \in \text{CWE}_{K,S}(t)$ must lie within $[0, \pi]$, i.e., $0 \leq \varphi(\mathbf{I} | \mathbf{I} \in \text{CWE}_{K,S}(t)) \leq \pi$. At **C** both the front and the back sides of the hemispherical surface of the cutter have engagements, and the total engagement area covers the full $[0, 2\pi]$ range, i.e., $0 \leq \varphi(\mathbf{I} | \mathbf{I} \in \text{CWE}_{K,S}(t)) \leq 2\pi$. The mapping will be developed for the most general case **C** where the hemispherical surface engages the workpiece in two regions—the front contact face $\text{CWE}_{K,S1}(t)$ and the back contact face $\text{CWE}_{K,S2}(t)$, where $\text{CWE}_{K,S}(t) = \text{CWE}_{K,S1} \cup \text{CWE}_{K,S2}$. Figure 11 shows the engagement regions and parameters (φ, d, L) for a point at \mathbf{I} on the hemispherical surface.

The mapping methodology is summarized in Fig. 12 and consists of four steps. The inputs are a point on the removal volume $\mathbf{I}(x_I, y_I, z_I) \in E^3$, the implicit representation of the cutter surface geometry G , and the parametric form of the tool path T_i .

Step 1. In this step the parameter value t along T_i is found. For a linear tool path, the tool tip coordinates with respect to tool path start $\mathbf{V}_S(x_S, y_S, z_S)$ and end $\mathbf{V}_E(x_E, y_E, z_E)$ points are given by

$$\mathbf{T}(t) = \mathbf{V}_S + (\mathbf{V}_E - \mathbf{V}_S)t, \quad 0 \leq t \leq 1 \quad (2)$$

For a BNEM the reference point at \mathbf{F} is chosen to be the center of the sphere. Its location can be expressed using the cutting tool tip coordinates as

$$\mathbf{F}(t) = \mathbf{T}(t) + r\mathbf{n} \quad (3)$$

where r and \mathbf{n} are the radius of the hemisphere and unit normal vector of the tool axis, respectively. When the hemispherical surface moves along a tool path, a family $G_S(t)$ of surfaces is generated. An expression for this family of surfaces is obtained by

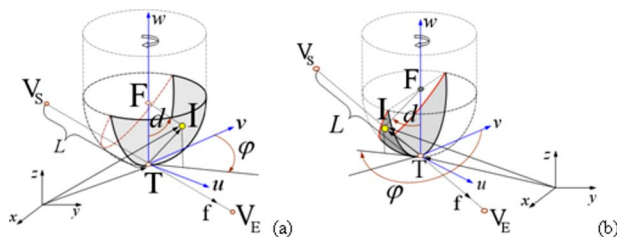


Fig. 11 Engagement regions of the (a) front and (b) back contact faces

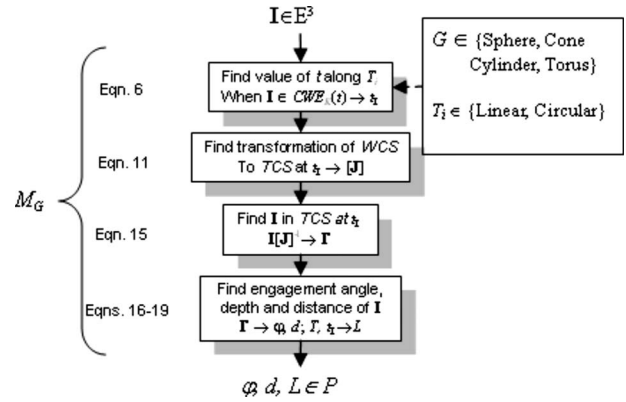


Fig. 12 Procedure for performing mapping $M_G: E^3 \rightarrow P(\varphi, d, L)$

substituting in the coordinates of the reference point at \mathbf{F} from Eq. (3) into the implicit form of a sphere given by Eq. (1a).

$$G_S(t): (\mathbf{P} - \mathbf{F}) \cdot (\mathbf{P} - \mathbf{F}) - r^2 = 0 \quad (4)$$

When the point at \mathbf{P} belongs to the set $\text{CWE}_{K,S}(t)$, Eq. (4) can be rewritten as

$$\text{CWE}_{K,S}(t): (\mathbf{I} - \mathbf{F}) \cdot (\mathbf{I} - \mathbf{F}) - r^2 = 0 \quad (5)$$

Given a point at \mathbf{I} that is known to be an engagement point, Eq. (5) can be expanded to take on the following quadratic form:

$$A_2 t^2 + A_1 t + A_0 = 0 \quad (6)$$

where the coefficients A_2 , A_1 , and A_0 are given by

$$A_2 = |\mathbf{V}_E - \mathbf{V}_S|^2$$

$$A_1 = -2[(\mathbf{I} - \mathbf{V}_S - r\mathbf{n}) \cdot (\mathbf{V}_E - \mathbf{V}_S)]$$

$$A_0 = |\mathbf{I} - \mathbf{V}_S - r\mathbf{n}|^2 - r^2 \quad (7)$$

Solving for t in Eq. (6) gives the position of the cutter tool tip when the point at \mathbf{I} is an engagement point between the cutter and the workpiece. In finding the correct tool position for an intersection point \mathbf{I} , the following property is used.

Property 3. Given a linear tool path T_i and the cutter surface geometry G for three-axis machining,

- (a) the maximum number of tool positions where the cutter touches a point in space is equal to the degree of the cutter surface geometry G ; i.e., the sphere is a degree of two surfaces;
- (b) if a point belongs to the removal volume then there is at least one cutter location where the cutter surface touches this point;
- (c) if the point is on the boundary of the swept volume SV_i of the cutter, there is a single tool position where the cutter surface touches this point.

The solution for Eq. (6) gives two real roots (Property 3 (a) and (b)) t_1 and t_2 where $t_1 \leq t_2$. These roots represent two possible cutter locations where the intersection point \mathbf{I} lies on the spherical surface, as shown in Fig. 13(a). To differentiate between the two choices and make the correct selection for t , the sign of the dot products $\mathbf{f} \cdot \mathbf{N}_1$ and $\mathbf{f} \cdot \mathbf{N}_2$ between the feed vector \mathbf{f} and the surface normals \mathbf{N}_1 and \mathbf{N}_2 for the two positions of the cutter is used. A negative value indicates that \mathbf{I} is in the shadow of the cutter and so cannot be a member of $\text{CWE}_K(t)$. For example, as shown in the figure, at location t_2 the dot product is negative, while at t_1 it is positive. It is easy to see that for linear tool motions, the smaller root of Eq. (6) should always be used.

For the special case where \mathbf{I} lies on the boundary of the swept volume of the cutter such that the scalar product $\mathbf{f} \cdot \mathbf{N}_1, \mathbf{N}_2 = 0$, the

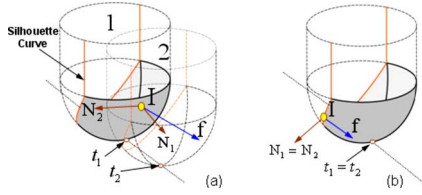


Fig. 13 Different cutter locations for $\mathbf{I} \in \text{CWE}_K(t)$

cutting tool has only one cutter location (Property 3 (c)), as shown in Fig. 13(b). The solution to Eq. (6) yields a repeated root, and \mathbf{I} satisfies the following system of equations, as shown in [18]

$$G_S(x_I, y_I, z_I, t) = 0, \quad \frac{\partial G_S(x_I, y_I, z_I, t)}{\partial t} = 0 \quad (8)$$

Step 2. Given the value of the tool path parameter $t=t_I$ when the cutter surface passes through \mathbf{I} , a transformation is created to map the global coordinate system (WCS) to a local tool coordinate system (TCS) at this location on the tool path. With the \mathbf{w} axis of cutter being one of the axes of the TCS, the \mathbf{v} axis (see Fig. 11) is obtained from the cross product of \mathbf{w} and the instantaneous feed direction vector $\mathbf{f}(t=t_I)$. The third axis \mathbf{u} is perpendicular to the first two,

$$\begin{aligned} \mathbf{v} &= (\mathbf{w} \times \mathbf{f}) / |\mathbf{w} \times \mathbf{f}| \\ \mathbf{u} &= (\mathbf{v} \times \mathbf{w}) / |\mathbf{v} \times \mathbf{w}| \end{aligned} \quad (9)$$

where

$$\mathbf{f} = (x_E - x_S)\mathbf{i} + (y_E - y_S)\mathbf{j} + (z_E - z_S)\mathbf{k} \quad (10)$$

Using Eq. (9) the transformation of a point in the TCS to one in the WCS is given by

$$\mathbf{I} = \mathbf{I}'[\mathbf{J}]_{t=t_I} \quad (11)$$

where

$$[\mathbf{J}]_{t=t_I} = \begin{bmatrix} \mathbf{u} & 0 \\ \mathbf{v} & 0 \\ \mathbf{w} & 0 \\ \mathbf{T}(t) & 1 \end{bmatrix}_{t=t_I} \equiv \begin{bmatrix} x_u & y_u & z_u & 0 \\ x_v & y_v & z_v & 0 \\ x_w & y_w & z_w & 0 \\ x(t)_T & y(t)_T & z(t)_T & 1 \end{bmatrix}_{t=t_I} \quad (12)$$

and \mathbf{I}' are the coordinates of \mathbf{I} in the TCS.

Step 3. To find $\varphi(t)$ and $d(t)$, the coordinates of an engagement point in the TCS is required. This is obtained from Eq. (11) as

$$\mathbf{I}' = \mathbf{I}[\mathbf{J}]_{t=t_I}^{-1} \quad (13)$$

Given that $[\mathbf{J}]_{t=t_I}$ is orthogonal, its inverse is defined by

$$[\mathbf{J}]_{t=t_I}^{-1} = \begin{bmatrix} x_u & x_v & x_w & 0 \\ y_u & y_v & y_w & 0 \\ z_u & z_v & z_w & 0 \\ -\mathbf{u} \cdot \mathbf{T}(t) & -\mathbf{v} \cdot \mathbf{T}(t) & -\mathbf{w} \cdot \mathbf{T}(t) & 1 \end{bmatrix}_{t=t_I} \quad (14)$$

Expanding Eq. (13) using Eq. (14) gives the coordinates of $\mathbf{I}'(x'_I, y'_I, z'_I)$. These are

$$\begin{aligned} x'_I &= \mathbf{I} \cdot \mathbf{u} - \mathbf{u} \cdot \mathbf{T}(t=t_I) \\ y'_I &= \mathbf{I} \cdot \mathbf{v} - \mathbf{v} \cdot \mathbf{T}(t=t_I) \\ z'_I &= \mathbf{I} \cdot \mathbf{w} - \mathbf{w} \cdot \mathbf{T}(t=t_I) \end{aligned} \quad (15)$$

Step 4. Given the coordinates of \mathbf{I}' on the hemispherical surface of the BNEM, its tool engagement angle $\varphi(t)$ is obtained using spherical coordinates. The engagement angle for the front contact face $\text{CWE}_{K,s1}(t)$ is given by

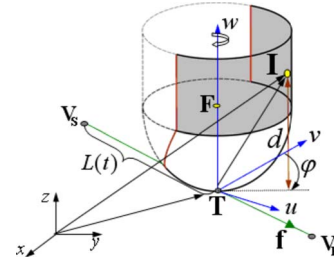


Fig. 14 Cylindrical contact face $\text{CWE}_{K,C}(t)$ of BNEM

$$\varphi(t=t_I) = \cos^{-1} \left(\frac{y'_I}{\sqrt{x_I'^2 + y_I'^2}} \right) \quad (16)$$

and for the back contact face $\text{CWE}_{K,s2}(t)$ is given by

$$\varphi(t=t_I) = 2\pi - \cos^{-1} \left(\frac{y'_I}{\sqrt{x_I'^2 + y_I'^2}} \right) \quad (17)$$

The depth of the engagement point for the spherical part is the angle from $\mathbf{T}(t)$ to \mathbf{I}' such that

$$d(t=t_I) = \cos^{-1} \left(1 - \frac{z'_I}{r} \right) \quad (18)$$

and finally the parameter $L(t)$ of \mathbf{I} is obtained using

$$L(t=t_I) = t|\mathbf{V}_E - \mathbf{V}_S| \quad (19)$$

3.1.2 Derivation of M_{cyl} for the BNEM. The mapping for the cylindrical surface of the ball end cutter is obtained, following the same steps just developed for the hemispherical cutter surface. It can be seen that except for the first, all steps and equations to accomplish the mapping remain the same. For the first step, the geometry of the cylinder changes Eq. (4) and (5) to

$$G_C(t): (\mathbf{P} - \mathbf{F}) \cdot (\mathbf{P} - \mathbf{F}) - [(\mathbf{P} - \mathbf{F}) \cdot \mathbf{n}]^2 - r^2 = 0 \quad (20)$$

and

$$\text{CWE}_{K,C}(t): (\mathbf{I} - \mathbf{F}) \cdot (\mathbf{I} - \mathbf{F}) - [(\mathbf{I} - \mathbf{F}) \cdot \mathbf{n}]^2 - r^2 = 0 \quad (21)$$

respectively (see Fig. 14), where r and \mathbf{n} are the radius of the cylindrical surface and the unit normal vector of the tool rotation axis, respectively. As with Eq. (6), Eq. (21) results in a quadratic equation in t when \mathbf{I} and \mathbf{F} are substituted. The solution to this and the remaining steps in the mapping procedure lead to the representation of a point \mathbf{I} on the cylindrical surface of the BNEM in (φ, d, L) coordinates. Detailed transformation formulas for the cylindrical end mill can be found in Appendix A.1.

3.2 Mapping M for BNEM and Circular Tool Path. In this section we highlight the mapping procedure for a circular tool path. The steps summarized in Fig. 12 can be followed with some important differences. One, in particular, is that the feed direction changes as a function of the tool path parametric variable t . This impacts the transformation from the WCS to the TCS. The parametric representation for the tool tip point for a circular tool path of radius R centered at $\mathbf{C}(x_C, y_C, z_C)$ is given by

$$\mathbf{T}(t) = \mathbf{C} + R \cos(t)\mathbf{d} + R \sin(t)\mathbf{e} \quad (22)$$

where $t \in [0, 2\pi]$ (see Fig. 15). $\mathbf{d}(x_d, y_d, z_d)$ and $\mathbf{e}(x_e, y_e, z_e)$ are two orthogonal unit vectors defining the plane of the circular tool path. Thus, this representation for \mathbf{T} is general even though circular interpolation on most milling machines is restricted to the XY , XZ , and YZ planes.

As with linear tool paths, the local tool coordinate system TCS defined with \mathbf{u} , \mathbf{v} , and \mathbf{w} has its origin at the tool tip point. The reference point \mathbf{F} is expressed in terms of the cutting tool tip coordinates using Eq. (3). Following the same steps outlined in

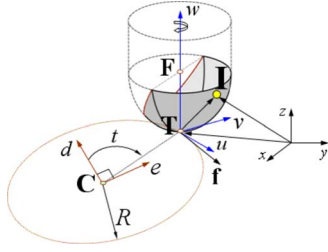


Fig. 15 Moving coordinate frame for the circular tool path

Sec. 3.1.1, Eq. (22) is substituted into Eq. (3), then into the implicit equation of the hemispherical surface of the cutter (Eq. (5)) with the coordinates of point **I** belonging to $CWE_K(t)$ obtained from the removal volume. The resulting equation can be expressed in terms of the parameter t in the following form:

$$A_2 \cos(t) + A_1 \sin(t) + A_0 = 0 \quad (23)$$

where A_2 , A_1 , and A_0 are constants for the current intersection point **I** given by the following expressions:

$$\begin{aligned} \mathbf{a} &= [(x_I - x_C - r_n)(y_I - y_C - r_n)(z_I - z_C - r_n)] \\ A_2 &= -2R(\mathbf{a} \cdot \mathbf{d}), \quad A_1 = -2R(\mathbf{a} \cdot \mathbf{e}), \quad A_0 = |\mathbf{a}|^2 + R^2 - r^2 \end{aligned} \quad (24)$$

Equation (23) in t can be written in the following form:

$$\sqrt{A_1^2 + A_2^2} \sin(t + \theta) + A_0 = 0 \quad (25)$$

where $\theta = \tan^{-1}(A_2/A_1)$. This leads to the following general equation for t :

$$t = -\theta + (-1)^n \alpha + n\pi, \quad \alpha = \sin^{-1}\left(\frac{-A_0}{\sqrt{A_1^2 + A_2^2}}\right) \quad (26)$$

where n is an integer. Define n_1 to be the smallest n such that $t > t_0$. Then n_1 can be calculated as

$$n_1 = \min\left(2\left\lceil \frac{\theta - \alpha + t_0}{2\pi} \right\rceil, 2\left\lfloor \frac{\theta + \alpha + t_0}{2\pi} - \frac{1}{2} \right\rfloor\right) \quad (27)$$

After n_1 is found, it can be incremented by unit steps to calculate the next tool tip point **T** for the given **I**. There can be up to two cutter location points in the interval for a given engagement point **I**. As explained in Sec. 3.1.1, the minimum root is selected. Having solved for the parameter t value when **I** is an engagement point, it is substituted into Eq. (22) to find the tool tip coordinates. The direction of the feed vector at this location is given by

$$\begin{aligned} \mathbf{f}(t = t_1) &= \frac{d\mathbf{T}}{dt} = R(-\sin(t)x_d + \cos(t)x_e)\mathbf{i} + R(-\sin(t)y_d + \cos(t)y_e)\mathbf{j} \\ &+ R(-\sin(t)z_d + \cos(t)z_e)\mathbf{k} \end{aligned} \quad (28)$$

Given \mathbf{f} and t , Eqs. (16)–(18) are used to find (φ, d) parameters for **I**, and $L(t)$ of **I** is obtained using

$$L(t = t_1) = R t \quad (29)$$

The mapping for the cylindrical portion of the cutter follows the same steps using the implicit surface for a cylinder.

3.3 Summary of Mappings for Other Cutter Surface Geometries. In addition to hemispherical and cylindrical surfaces mappings have also been developed for conical and toroidal cutter surfaces moving along linear tool path. As illustrated above the primary difference that a new surface geometry introduces is in finding the value of the parameter t corresponding to an engagement point **I**. The remaining steps in the procedure are the same. A summary of the key equations for combinations of these additional surfaces is included in the Appendix.

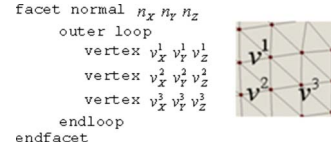


Fig. 16 STL file structure and facets

4 Implementation

In this research the mappings developed in the previous section are applied directly to a polyhedral representation of the removal volume. The specific representation utilized is the “stereo lithography” (STL) format although other representations (VRML, .jt, .hsf, etc.) can as easily be adopted. In the STL representation, the geometry of surfaces is represented by small triangles called facets. These facets are described by three vertices and the normal direction of the triangle, as shown in Fig. 16.

To test the methodology for CWE extraction, a prototype system has been assembled using existing commercial software applications and C++ implementations of the mapping procedure described above. This system is shown in Fig. 17. Tool motion simulation based on CLData is performed using VERICUT,¹ a commercial NC verification application. This application uses a voxel-based model to capture changes to the in-process workpiece. STL representations of in-process workpiece states can be generated from the voxel representation prior to any tool path motion in the CLData file.

Not currently available through the programable APIs provided for customization is a function for outputting STL representations of removal volumes. However, this is probably an easy extension to implement. Thus, to obtain removal volumes for a given tool motion the ACIS software² is utilized to model a B-rep solid of the associated swept volume. These swept volumes are exported to the STL format. A Boolean intersection between this swept volume and the current in-process workpiece output from VERICUT is performed using the polyhedral modeling Boolean operators implemented in a third commercial application, MAGICS X.³ Though currently a manual process, this prototype system creates STL models of removal volumes generated during the machining of complex components. It utilizes the same CAD/CAM data generated for machining the part.

5 Results

In this section examples of the application of the mapping M to removal volumes generated by different types of cutting tools and tool motions are presented. The first set of examples is designed to demonstrate the generality of the approach with respect to tool geometry and linear and circular tool motions. The second set comes directly from applying the prototype system described in the previous section to CAD/CAM data created in machining a gearbox cover. This demonstrates the practicality of the methodology.

5.1 Example Set 1. In this example set different cutting tools and simple linear and circular tool motions are presented to demonstrate the generality of the approach. Figures 18 and 19 show ball nose and flat end mills removing material along a linear ramping tool path; i.e., the tool moves in all three axes simultaneously. In each case the original and transformed removal volumes are given. The removal volumes associated with the different cutter surfaces are separated. In the case of the flat end mill, this gives the material removed by the cylindrical (side face) and

¹VERICUT is developed and marketed by CGITech Inc.

²ACIS is a geometric/solid modeling kernel developed by Spatial Technologies a subsidiary of Dassault Systemes.

³MAGICS X is a process planning system for rapid prototyping developed by Dimensionalize.

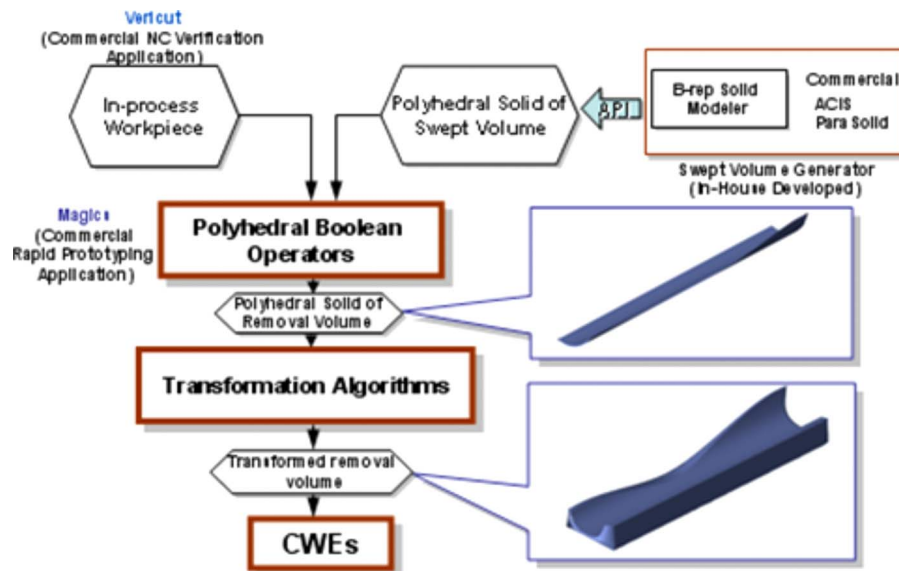


Fig. 17 Implementation of CWE extraction methodology

flat (bottom face) cutter surfaces. Plots of CWEs at different CLs along the tool path are illustrated. These are obtained by intersecting the transformed removal volume with a plane representing the cutting tool. Two formats for plotting the CWEs are used. The first is an XY plot of depth of cut (as measured from the tool tip point) versus engagement angle. The second plot shows the engagement area of the cutter bottom surface (Fig. 19) in a polar format. In the linear ramping example of the ball nose end mill, the plots show that engagement of the cutter occurs over the full range, i.e., $[0, 2\pi]$. Between zero and π , the engagement is due to the front contact face (the CWE in this zone is divided to illustrate this) and

between π and 2π due to the back contact face.

For the flat end mill XY plots show the engagement between zero and π for the side face, and polar plots show the engagement between zero and 2π for the bottom face. The final example (Fig. 20) demonstrates the transformation as applied to a circular $21/2D$ tool path. These results together show that the mapping methodology reduces various combinations of cutter and tool path geometry to a generic form to which a single intersection operator can be applied.

5.2 Example Set 2. The examples in this section are created

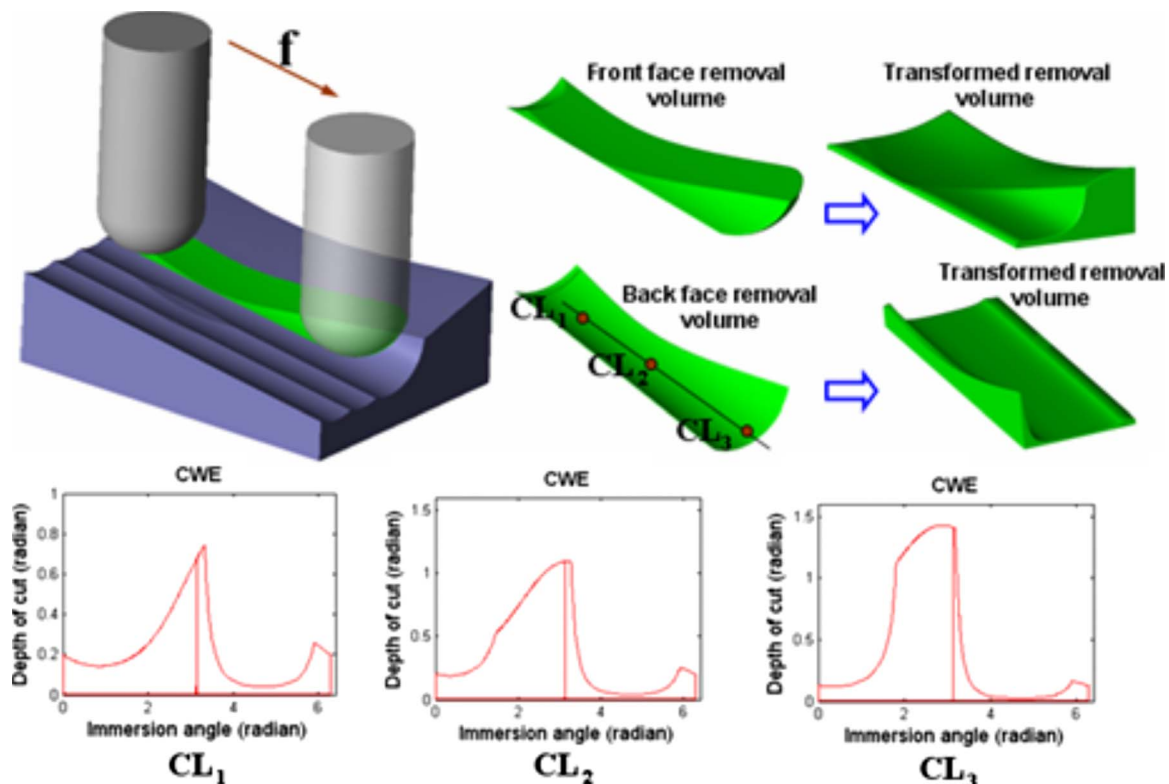


Fig. 18 CWEs for ball nose end mill performing a linear three-axis move

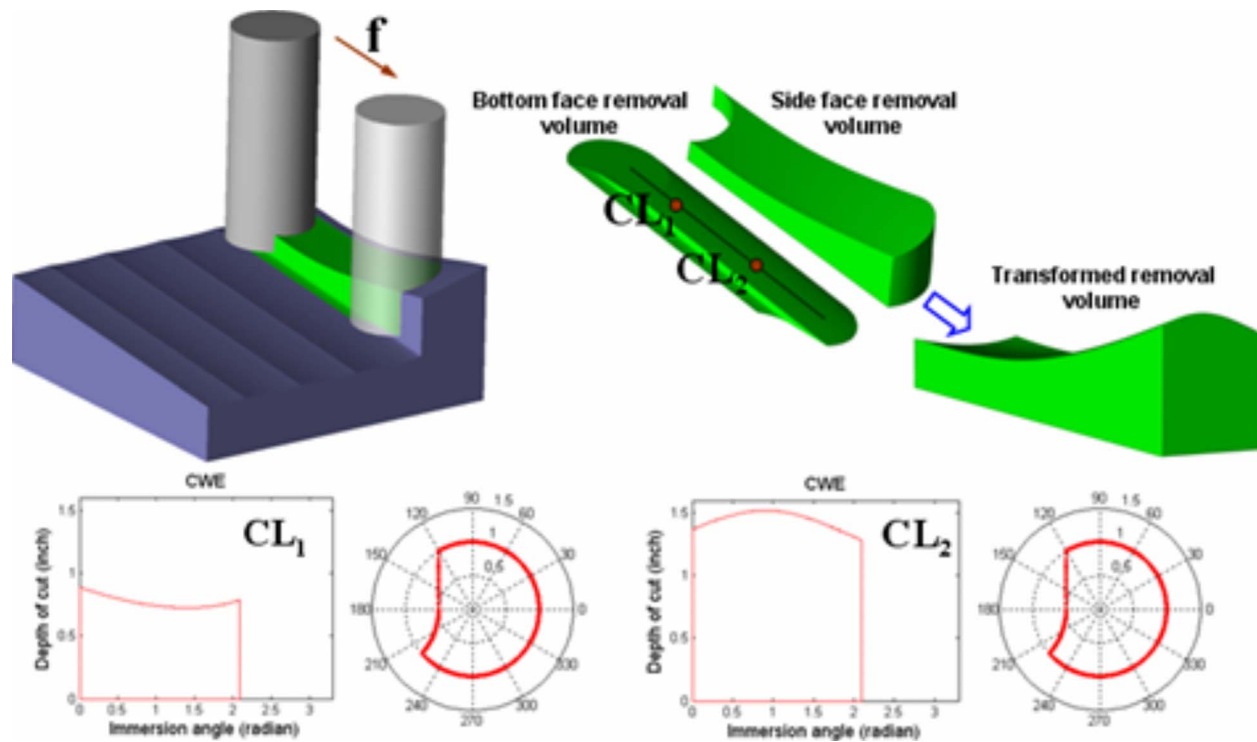


Fig. 19 CWEs for flat end mill performing a linear three-axis move

using the steps outlined in Sec. 4. The CAD model and tool paths for machining were both created using Unigraphics NX3. Figure 21 shows the in-process workpiece of a gearbox cover and the removal volume for the next tool path generated by VERICUT, ACIS, and MAGICS. The removal volume generated by the ball nose end mill clearly shows the complicated removal volume shapes and resulting CWEs that can be generated when machining complex parts.

Figure 22 shows a circular milling operation for enlarging a

hole. In this example the side face of the flat end mill removes the material, and its removal volume is shown. The cutter performs a half turn, which corresponds to a 0–180 deg range.

6 Discussion and Future Work

In this paper a robust and efficient method for obtaining CWEs using faceted models, which are used extensively in simulation, CAE, and rapid prototyping, is presented. A mapping technique

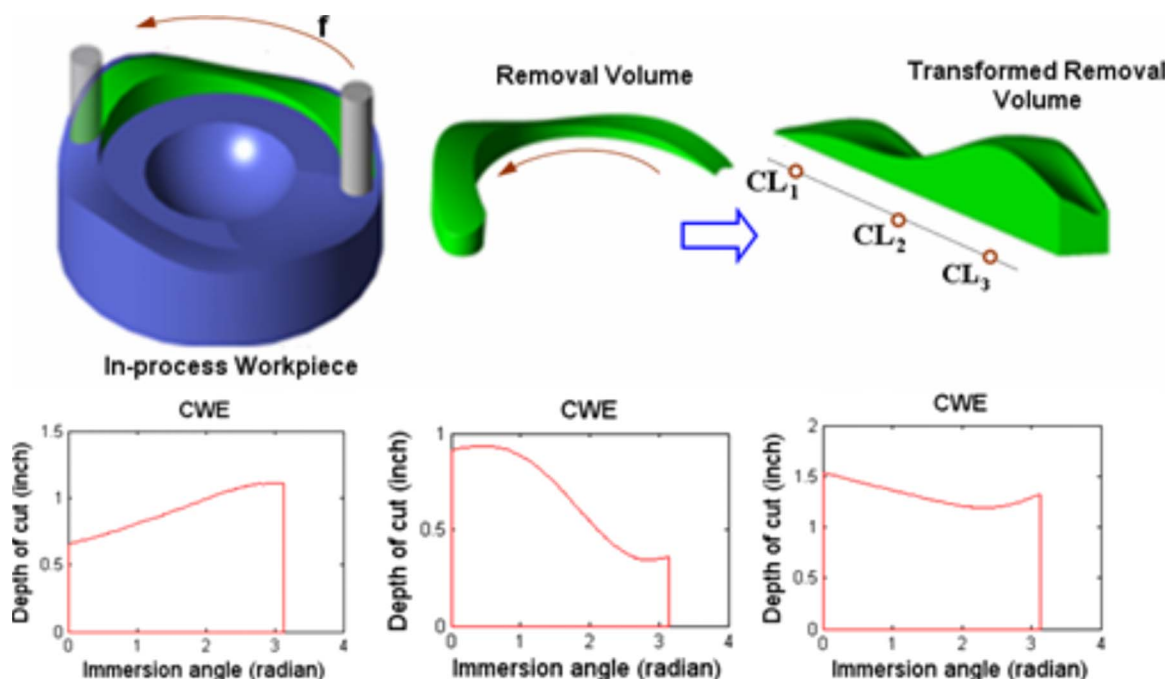


Fig. 20 CWEs for flat end mill performing a circular move

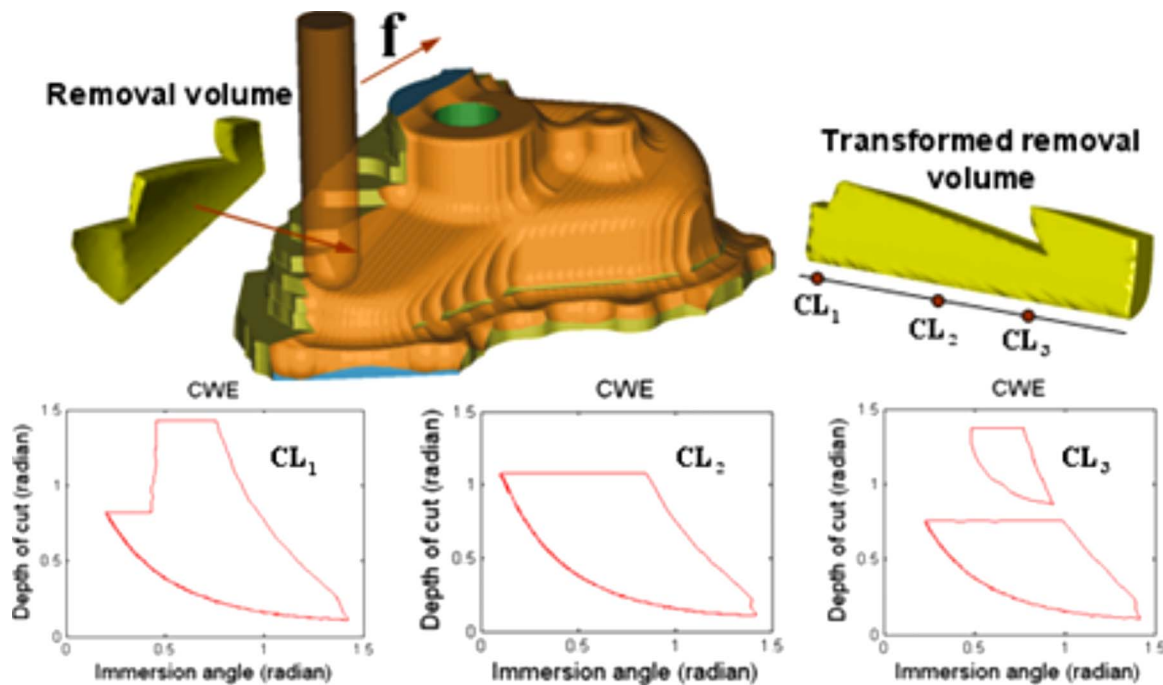


Fig. 21 CWEs for ball end mill performing a linear three-axis move

has been developed that transforms a polyhedral model of the removal volume from a Euclidean space to a parametric space, which is defined by the *cutter engagement angle*, depth of cut, and *cutter location*. This mapping methodology brings some important advantages over other approaches. First, it is purely analytical due to the reduction of the complexity in the CWE calculations to first order plane-plane intersections. When compared to other polyhedral modeling approaches, it has greater robustness because it addresses the chordal error problem found in intersecting polyhedral models.

To reduce the size of the data structure that needs to be manipulated, the removal volume is used instead of the in-process workpiece. This approach also has the potential of being implemented using a parallel processing strategy [19]. For the CWE extractions common milling cutting tools, which are natural quadrics consisting of the sphere, the circular cylinder, and the cone together with the torus, are used. This method can also be applied to other types of cutting tool geometries which have implicit representations such as cutters with paraboloid, spheroid, or hyperboloid surfaces.

In this research it is assumed that the size of the facets in the removal volume is sufficiently small so as not to introduce significant errors in the CWE boundaries. To study this a comparison is made between engagements obtained from intersecting the removal volume using a B-rep solid modeler (the most accurate approach) and those from the polyhedral approach described in this paper using different faceting resolutions. Examples of removal volumes for both representations are shown in Figs. 23(a) and 23(b), respectively. CWEs are obtained for cutter locations CL_1 – CL_{29} . For CL_5 the CWEs from the solid modeler (Fig. 23(c)) and polyhedral modeler at facet resolutions of 2 mm (Fig. 23(d)) and 6 mm (Fig. 23(e)) are shown. To compare the effects of the size of the facets, the CWE area is decomposed using a QuadTree [20] spatial data structure (Fig. 23(f)).

The area of the CWE is obtained by accumulating the square areas that lie within the QuadTree representation of the CWE boundary. For each CL point the areas obtained from the different resolutions are compared with that of the B-rep solid modeler

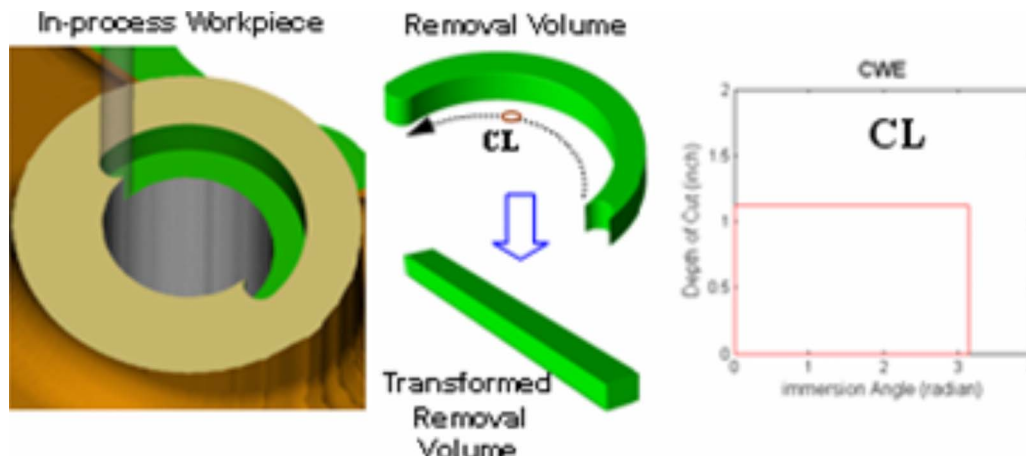


Fig. 22 CWE for flat end mill performing a circular move

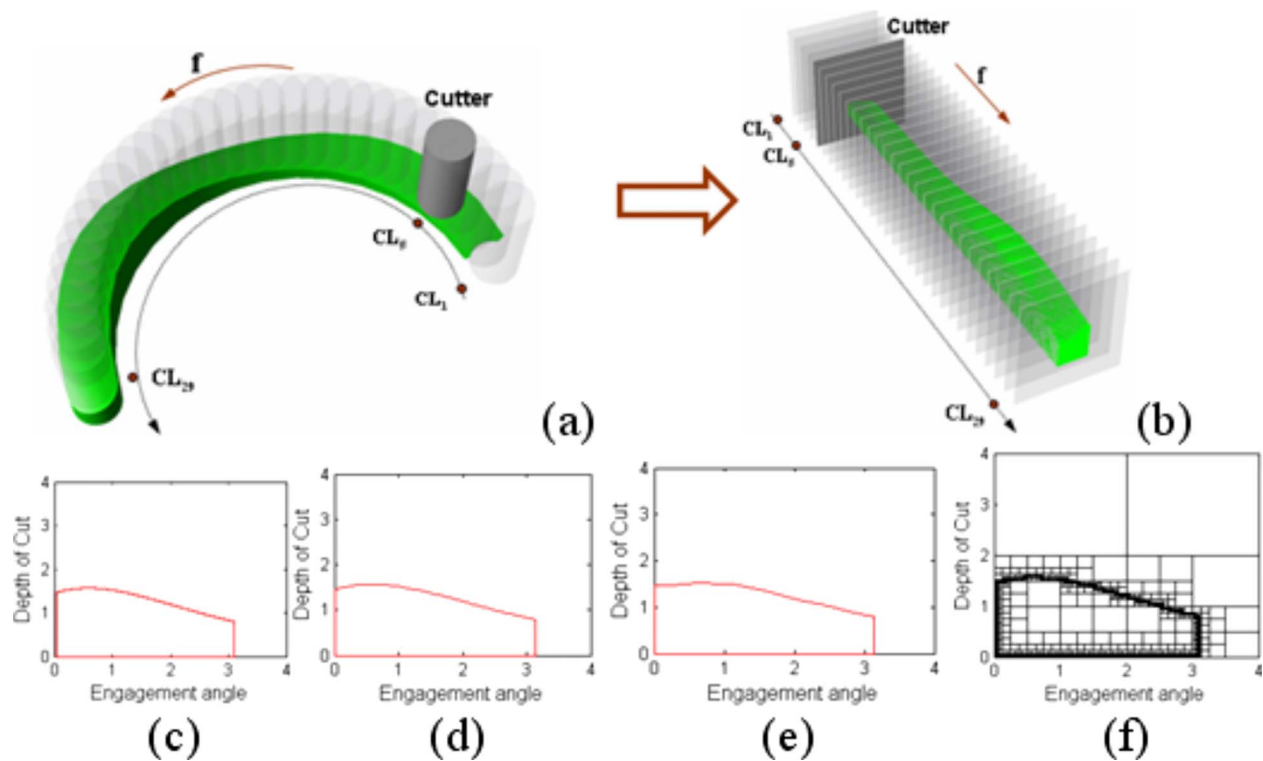


Fig. 23 (a) and (b) removal volumes and (c)–(f) CWEs for different resolutions

(Fig. 24(a)). The graph shows a 4% error at 6 mm and less than 1% at 2 mm. Figure 24(b) shows the facet size versus intersection time; i.e., the time for obtaining the CWE area for a given cutter location point is shown. While the absolute value would vary depending on the implementation, the trend should remain the same. This shows that there is a small increase in the intersection time as the resolution is decreased from 6 mm to 2 mm after which it increases significantly. Both the error and intersection time results point to 2 mm being a practical limit for the facet size in this example. We point out that this limit will vary depending on the cutter size. An expression needs to be developed to calculate the resolution that considers this parameter.

In this work the mapping between a point in the Euclidian space and one in the parametric space is assumed to be one to one for the circular tool path. Volumes with self-intersections violate this assumption. For example when the cutter radius is greater than the circular path radius, a condition that occurs for circular

hole milling, the volume is always self-intersecting. Modifications to the methodology will need to be developed for this special case. Like the kinematics, when the tool path complexity increases, extracting CWEs becomes computationally more expensive. The modeling of other kinds of tool paths such as spirals, trochoids, and splines using the transformation methodology will be investigated.

The authors also believe that the approach can be used for other types of tool paths (helical, spiral, circular milling, etc.) and for a five-axis machining with some modifications. This is currently one direction of research. Finally, a stand-alone polyhedral based CWE extraction approach that replaces the various commercial components shown in Fig. 17 will be developed. The authors view this more as a matter of implementation since many of the techniques needed are part of existing commercial packages, as has been demonstrated.

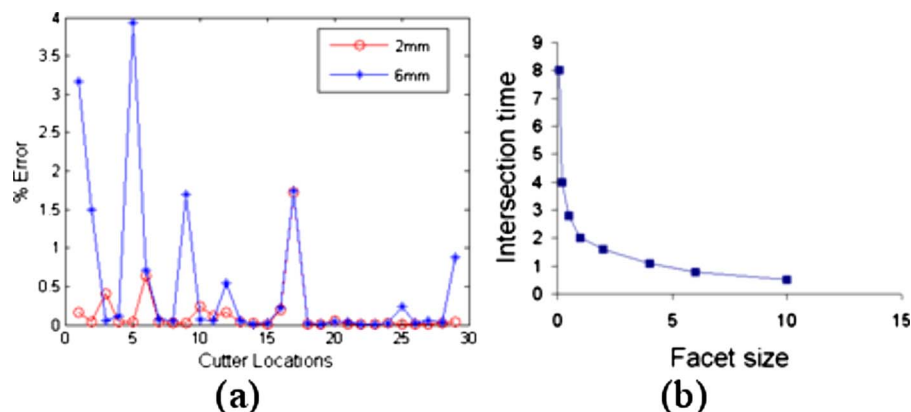


Fig. 24 The effect of the facet resolutions

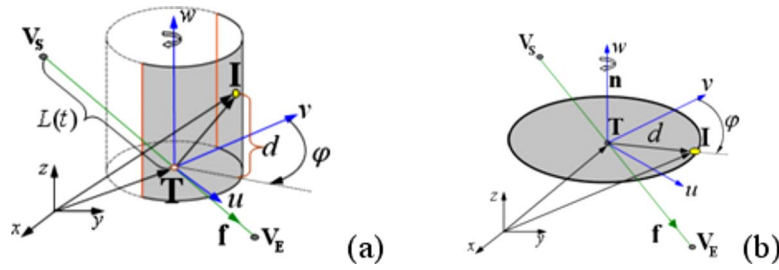


Fig. 25 Engagement regions of the (a) cylindrical and (b) flat contact faces for the flat end mill

7 Conclusions

The methodology presented in the paper targets the important problem of finding CWEs for milling. It is based on a polyhedral representation of the removal volume, which is mapped from a Euclidean space to a parametric space defined by the location along the tool path, the engagement angle, and the depth of cut. This simplifies the intersection calculations to those between planar surfaces. Examples have been presented to show that the approach generates proper engagements. The method can be generalized to other types of machining kinematics and cutting tools. The described mapping technique is being developed as part of a virtual milling methodology that combines the geometric modeling aspects of milling material removal with the modeling of the process.

Acknowledgment

The authors would like to acknowledge the support of NSERC and Pratt and Whitney Canada in this research.

Nomenclature

- T_i = tool path for the i th tool motion
- SV_i = swept volume generated for the i th tool motion in E^3
- RV_i = removal volume generated for the i th tool motion in E^3
- M = a transformation that maps RV_i from E^3 to $P(\varphi, d, L)$ i.e., $M: E^3 \rightarrow P(\varphi, d, L)$
- SV_i^P = the map of SV_i in $P(\varphi, d, L)$
- RV_i^P = the map of RV_i in $P(\varphi, d, L)$
- $N(\varnothing, \beta)$ = surface normal of a point on cutter ($0 \leq \varnothing, \beta \leq 1$)
- $CWE_K(t)$ = the set of all points on the surface of a cutter at location t along a tool path where $\mathbf{f} \cdot \mathbf{N} \geq 0$. These are kinematically feasible engagement points for a given instantaneous feed vector $\mathbf{f}(t)$
- $CWE(t)$ = the set of all points on the surface of a cutter at location t along a tool path that are engaged with the workpiece
- $bCWE(t)$ = points on the boundary of $CWE(t)$

Appendix A

For the following derivations the tool motion type C in Fig. 10 is used.

A.1 Derivation of M_{cyl}

A flat end mill is made up of a cylindrical surface at the side and a flat surface at the bottom (Figs. 25(a) and 25(b)). For the cylindrical surface the engagement angle of a point at \mathbf{I} must lie within $[0, \pi]$, and for the flat surface it must lie within $[0, 2\pi]$. For the cylindrical surface the tool reference point \mathbf{F} is selected to

be the tool tip point in Eq. (2), i.e., $\mathbf{F}(t) = \mathbf{T}(t)$. Equation (21) results in a quadratic equation in t when \mathbf{I} and \mathbf{F} are substituted. Two real roots of Eq. (21) represent two cutter locations, and as explained in Sec. 3.1.1, the minimum root is selected to be the correct tool position.

Using Eqs. (16) and (19), the parameters φ and L are obtained. Finally, the depth of the engagement point, as defined by the distance from $\mathbf{T}(t)$ to \mathbf{I}' measured along the tool axis vector, is simply the z -coordinate of \mathbf{I}' ,

$$d(t) = z'_I = \mathbf{I} \cdot \mathbf{w} - \mathbf{w} \cdot \mathbf{T}(t) \quad (A1)$$

CWE parameters for the flat surface are obtained without doing a mapping. An unbounded plane, which is perpendicular to the tool rotation axis, is intersected with the original removal volume of the bottom surface for a given cutter location point. An engagement angle φ is found by Eqs. (16) and (17). The depth of the cut for the bottom surface is the distance between the intersection point \mathbf{I} and the center of the bottom surface such that

$$d = \sqrt{x_I'^2 + y_I'^2} \quad (A2)$$

A.2 Derivation of M_{cone}

The conical surface of a tapered flat end mill is made up of front and back conical contact faces on the sides (Figs. 26(a) and 26(b)) and a flat surface at the bottom. For the given tool motion type C in Fig. 10, the cutter has engagements with all its surfaces, and the total engagement area covers the full $[0, 2\pi]$ range. The tool reference point \mathbf{F} is chosen to be the tool tip point in Eq. (2). For the first step, the geometry of the cone changes Eq. (5) to

$$CWE_{K,Co}: (\mathbf{I} - \mathbf{V}) \cdot (\mathbf{I} - \mathbf{V}) - (1 + \tan^2 \alpha) \{(\mathbf{I} - \mathbf{V}) \cdot \mathbf{n}\}^2 = 0 \quad (A3)$$

where α , \mathbf{n} , and \mathbf{V} are the cone half angle, unit normal vector of the tool rotation axis, and cone vertex coordinates, respectively. The relationship between \mathbf{V} and \mathbf{F} is given by

$$\mathbf{V} = \mathbf{F} - \frac{r}{\tan \alpha} \mathbf{n} \quad (A4)$$

where r is the bottom radius of the conical frustum surface. As with Eq. (6), Eq. (A3) results in a quadratic equation in t when \mathbf{I} and \mathbf{F} are substituted. Two real roots of Eq. (A3) represent two cutter locations, and as explained in Sec. 3.1.1 the minimum root is selected to be the correct tool position. Using Eqs. (16), (17), (19), and (A1), the parameters (φ, d, L) are obtained. CWE parameters of the flat surface are obtained in the same way as explained in Appendix A.1.

A.3 Derivation of M_{torus}

The toroidal portion of a bull-nose end mill is made up of front and back contact faces at the side (Figs. 27(a) and 27(b)) and a flat surface at the bottom. The reference point at \mathbf{F} is chosen to be the center of the torus. Its location can be expressed by the cutting tool tip coordinates as

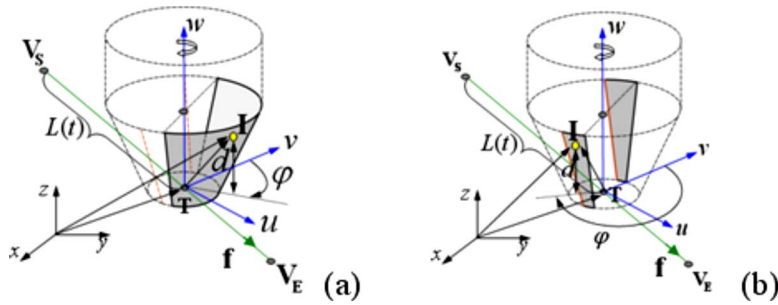


Fig. 26 Engagement regions of the (a) front and (b) back contact faces for the tapered flat end mill

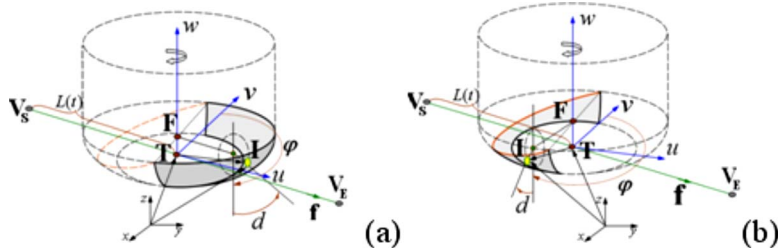


Fig. 27 Engagement regions of the (a) front and (b) back toroidal contact faces for the toroidal end mill

$$\mathbf{F}(t) = \mathbf{T}(t) + r\mathbf{n} \quad (\text{A5})$$

where r and \mathbf{n} are the radius of tube and the unit normal vector of the tool axis, respectively.

For the first step, the geometry of the torus changes Eq. (5) to

$$\text{CWE}_{K,T}: \{(\mathbf{I} - \mathbf{F}) \cdot (\mathbf{I} - \mathbf{F}) - r^2 - R^2\}^2 + 4R^2\{(z - z_R)^2 - r^2\} = 0 \quad (\text{A6})$$

Equation (A6) results in a quartic fourth order polynomial equation in t when \mathbf{I} and \mathbf{F} are substituted and gives four roots. According to Property 3, the toroidal surface has a maximum of four cutter locations for \mathbf{I} . For example, two CWE points \mathbf{I}_1 and \mathbf{I}_2 are shown in Fig. 28. Along the tool path the toroidal surface touches point \mathbf{I}_1 at four different contact points, i.e., $\mathbf{T}_1, \mathbf{T}_2, \mathbf{T}_3, \mathbf{T}_4$. Thus for \mathbf{I}_1 Eq. (A6) gives four distinct real roots such that $t_1 < t_2 < t_3 < t_4$, and as explained in Sec. 3.1.1 the minimum of these is taken to be the tool location when cutter touches this point. The toroidal surface touches \mathbf{I}_2 at the contact point \mathbf{T}_5 , and because \mathbf{I}_2 is on the envelope surface of the cutter, Eq. (A6) gives repeated real roots for \mathbf{I}_2 .

Using Eqs. (16), (17), and (19), (φ, L) parameters are found. The depth of the engagement point is obtained by

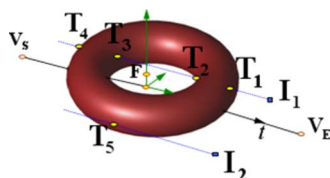


Fig. 28 Cutter interferences with points in space

$$d(t) = \cos^{-1} \left(1 - \frac{z'_t}{r} \right) \quad (\text{A7})$$

The CWE parameters of the flat surface are obtained in the same way as explained in Appendix A.1.

References

- [1] Fussell, B. K., Jerard, R. B., and Hemmett, J. G., 2003, "Modeling of Cutting Geometry and Forces for 5-Axis Sculptured Surface Machining," *Comput.-Aided Des.*, **35**, pp. 333–346.
- [2] Choi, B. K., and Jerard, R. B., 1998, *Sculptured Surface Machining: Theory and Applications*, Kluwer Academic, Dordrecht, The Netherlands.
- [3] Jerard, R. B., Drysdale, R. L., Hauck, K. E., Schaudt, B., and Magewick, J., 1989, "Methods for Detecting Errors in Numerically Controlled Machining of Sculptured Surfaces," *IEEE Comput. Graphics Appl.*, **9**(1), pp. 26–39.
- [4] Fussell, B. K., Jerard, R. B., and Hemmett, J. G., 2001, "Robust Feedrate Selection for 3-Axis, NC Machining Using Discrete Models," *ASME J. Manuf. Sci. Eng.*, **123**, pp. 214–224.
- [5] Drysdale, R. L., Jerard, R. B., Schaudt, B., and Hauck, K., 1989, "Discrete Simulation of, NC Machining," *Algorithmica*, **4**, pp. 33–60.
- [6] Yun, W.-S., Ko, J. H., Lee, H. U., Cho, D.-W., and Ehmann, K. F., 2002, "Development of a Virtual Machining System, Part 3: Cutting Process Simulation in Transient Cuts," *Int. J. Mach. Tools Manuf.*, **42**(15), pp. 1617–1626.
- [7] Kim, M. G., and Chu, N. G., 2004, "Mean Cutting Force Prediction in Ball-end Milling Using Force Map Method," *J. Mater. Process. Technol.*, **146**, pp. 303–310.
- [8] Gupta, S. K., Saini, S. K., Brent, W. S., and Yao, Z., 2005, "Geometric Algorithms for Computing Cutter Engagement Functions in 2.5D Milling Operations," *Comput.-Aided Des.*, **37**, pp. 1469–1480.
- [9] Wang, W. P., 2005, "Solid Modeling for Optimizing Metal Removal of Three Dimensional, NC End Milling," *J. Manuf. Syst.*, **7**(1), pp. 57–65.
- [10] Spence, A. D., and Altintas, Y., 1994, "A Solid Modeler Based Milling Process Simulation and Planning System," *ASME J. Eng. Ind.*, **116**(1), pp. 61–69.
- [11] Spence, A. D., and Li, Z., 2001, "Parallel Processing for 2-1/2, D Machining Simulation," *ACM Symposium on Solid Modeling and Applications*, pp. 140–148.
- [12] El-Mounayri, H., Elbestawi, M. A., Spence, A. D., and Bedi, S., 1997, "General Geometric Modeling Approach for Machining Process Simulation," *Int. J. Adv. Manuf. Technol.*, **13**, pp. 237–247.
- [13] Sadeghi, M. H., Haghighat, H., and Elbestawi, M. A., 2003, "A Solid Modeler Based Ball-End Milling Process Simulation," *Int. J. Adv. Manuf. Technol.*, **22**, pp. 775–785.
- [14] Weinert, K., and Surmann, T., 2003, "Geometric Simulation of the Milling

Process for Free Formed Surfaces," *Conference Proceedings: Simulation Aided Offline Process Design and Optimization in Manufacturing Sculptured Surfaces*, Witten Bommerholz, K. Weinert, ed., pp. 21–30.

- [15] Larue, A., and Altintas, Y., 2005, "Simulation of Flank Milling Processes," *Int. J. Mach. Tools Manuf.*, **45**, pp. 549–559.
- [16] Yip-Hoi, D., and Huang, X., 2006, "Cutter/Workpiece Engagement Feature Extraction From Solid Models for End Milling," *ASME J. Manuf. Sci. Eng.*, **128**(1), pp. 249–260.
- [17] Yao, Z., 2005, "Finding Cutter Engagement for Ball End Milling of Tesellated

Free-Form Surfaces," *Proceedings of IDETC/CIE ASME International Design Engineering Technical Conferences*.

- [18] Zeng-Jia, Hu., and Zhi-Kui, L., 1996, "Swept Volumes Generated by the Natural Quadric Surfaces," *Comput. Graph.*, **20**(2), pp. 263–274.
- [19] Wang, J., Peng, X., and Yip-Hoi, D., 2006, "A Multi-Agent System for Distributed, Internet Enabled Cutter/Workpiece Engagement Extraction," *Proceedings of the ASME Design Engineering Technical Conference*.
- [20] Samet, H., 1984, "The Quadtree and Related Hierarchical Data Structures," *ACM Comput. Surv.*, **16**(2), 187–260.